Christian-Albrechts-University, Kiel
Faculty of Mathematics and Natural Sciences

Characterizing mesoscale eddies in the Labrador Sea based on data from moored observations

Thesis
Master of Science Programme
Climate Physics: Meteorology and Physical Oceanography

Tobias Kunst
Matriculation Number: 1105582

Advisor: Dr. Johannes Karstensen
Co-Advisor: Prof. Dr. Martin Visbeck

Kiel, June 15th, 2023

GEOMAR Helmholtz Centre for Ocean Research Kiel

Abstract

In the Labrador Sea, mesoscale eddies have been identified as a major exchange agent between the fast flowing boundary currents and the quiescent interior Labrador Sea. This way, the eddies contribute to heat, freshwater and property fluxes and impact deep convection and carbon uptake. It is therefore of interest to carefully analyse the occurrence, dynamics and water mass characteristics of mesoscale eddies in the Labrador Sea.

Here, four years of moored instrument time series data are analyzed for eddy occurrences. A semi-automatic method for eddy detection in moored velocity data was developed and the eddie's time series data were fit to a Rankine vortex model in order to estimate eddy characteristics. Over the four years, three cyclonic and seven anticyclonic eddies have been detected with this method. Surprisingly, most eddies differ in their characteristics and structures from the eddies reported in earlier studies, namely Irminger Rings, Convective Eddies, and Boundary Current Eddies. In particular, no Irminger Ring was found but a cyclonic, bottom-intensified warm core eddy, which has not been reported in this area before.

Zusammenfassung

In der Labradorsee wurden mesoskalige Wirbel als wichtiger Austauschmechanismus zwischen den schnell fließenden Randströmungen und dem ruhigen Inneren der Labradorsee identifiziert. Auf diese Weise tragen die Wirbel zu Wärme und Süßwasser-flüssen bei und sorgen für einen Austauch von Wassereigenschaften, die die Tiefenkonvektion und die Kohlenstoffaufnahme beeinflussen. Daher ist es von Interesse, das Auftreten, die Dynamik und Wassermasseneigenschaften von mesoskaligen Wirbeln in der Labradorsee sorgfältig zu analysieren.

Hier werden vier Jahre an Zeitserien von Verankerungsdaten auf das Auftreten von Wirbeln analysiert. Es wurde eine halbautomatische Methode zur Wirbelerkennung entwickelt und die Zeitreihendaten der Wirbel wurden an ein Rankine-Wirbelmodell angepasst, um Eigenschaften der Wirbel abzuschätzen. Über die vier Jahre hinweg wurden mit dieser Methode drei zyklonale und sieben antizyklonale Wirbel entdeckt. Überraschenderweise unterscheiden sich die meisten Wirbel in ihren Eigenschaften und Strukturen von den Wirbeln, über die in früheren Studien berichtet wurde, namentlich Irminger Ringe, 'Convective Eddies' und 'Boundary Current Eddies'. Insbesondere wurde kein Irminger Ring gefunden, aber ein zyklonaler 'bottom-intensified' Wirbel mit warmen Kern, der in diesem Gebiet bisher noch nicht beobachtet wurde.

Contents

1 Introduction

1.1 The Labrador Sea

The Labrador Sea in the subpolar Atlantic is located between the west coast of Greenland and the Labrador Peninsula of Canada. The cyclonic boundary current system of the Labrador Sea consists of three currents of different origin (see Fig. 1). The West Greenland Current (WGC) flows northward along the Greenland shelf and is accompanied by the warm and salty subsurface Irminger Current (IC), which carries waters from subtropical regions into the Labrador Sea and acts as a heat source (Cuny et al., 2002). The cold and fresh Labrador Current (LC) flows southwards along the western coast, transporting waters from the Arctic Ocean. The North Atlantic Current (NAC) acts as a southern boundary to the circulation.

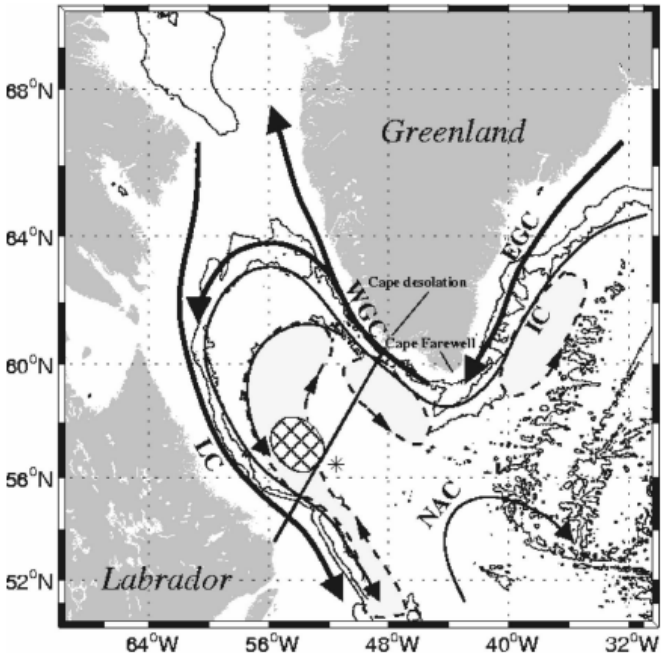

Figure 1: Taken from Chanut et al. (2008): Overview over the circulation in the Labrador Sea. WGC for West Greenland Current, IC for Irminger Current, LC for Labrador Current, NAC for North Atlantic Current. The shaded area marks the convection site after Pickart (2002). The star marks the location of the OWS Bravo, which is close to the study area of this thesis.

Several studies highlight the role of the Labrador Sea in the thermohaline circulation, as it is one of the few areas in the world in which open-ocean deep convection and the associated formation of Labrador Sea Water occurs in a repeating annual cycle. This convection cycle happens in three phases (Marshall & Schott, 1999): (1) A Preconditioning of the water column, (2) the deep convection and (3) a rapid restratification of the water column.

The surface waters in the central Labrador Sea are essentially isolated by the boundary currents and it is characterized by very weak interior flow (Lavender et al., 2000). The cyclonic gyre formed by the boundary currents additionally causes a doming of isopycnals, bringing weakly stratified water to the surface. During wintertime, strong and cold winds from arctic origin meets the comparatively warm water in the Labrador Sea, causing large air-sea heat fluxes and a buoyancy loss at the surface, until deep convection sets in and Labrador Sea Water is formed (Clarke & Gascard, 1983). The size of this convective patch can reach a horizontal extent of up to $200km$ and up to $2000m$ deep (Chanut et al. 2008). After convection, a lateral exchange of water from the convective patch with more buoyant water from the boundary currents leads to a rapid restratification of the water column (Gascard & Clarke, 1983). This lateral exchange of waters does not only occur directly after convection, but persists throughout the year, overall balancing the heat loss experienced through air-sea heat fluxes (Straneo, 2006). This exchange is driven by mesoscale eddies which are formed through instabilities in the boundary currents and propagate into the basin (Lilly et al., 2003, Katsman et al., 2004), acting as a core mechanism of heat transport in the Labrador Sea.

While the strength, spacial extent and location of deep convection exhibits interannual variability, which is closely connected to the variability in the atmospheric forcing (Pickart et al., 2002) and the strength of the subpolar gyre (Treguier et al., 2005), several studies suggest that eddies also have a significant impact on the variability by directly affecting preconditioning and restratification (Chanut et al., 2008; Rieck et al., 2019).

1.2 Eddy characteristics

The lateral exchange of water masses between the boundary currents and the central Labrador Sea is driven by mesoscale eddies, which are vortices formed through barotropic or baroclinic instabilities. Eddies can be described by their characteristics like rotational sense (anticylonic/cyclonic), size, maximum azimuthal velocities and the depth in which the flow is the strongest, and by the water properties that they carry with them (temperature, salinity).

In the Labrador Sea, three types of eddies are commonly found, namely Irminger Rings, convective eddies and boundary current eddies (see Chanut et al., 2008)

Irminger Rings (IR) are generated near Cape Desolation, where the topography redirects the West Greenland Current and induces instabilities with the Irminger Current,

causing the generation of eddies (Eden & Böning, 2002). IRs are very energetic anticyclones and are characterized by a warm and salty core close to the surface (Lilly et al., 2003). Some observations contrarily report a cap of cold and fresh water above the core instead (Hátún et al., 2007). Different observational studies found IRs with radii in the range of 11 to $35km$ and maximal azimuthal velocities of 14 to $77cm\,s^{-1}$, with surface intensified currents (Lilly et al., 2003; de Jong et al., 2014). In a model study, Chanut et al. (2008) find that IRs are generally confined to the northern part of the Labrador Sea, where they increase the stratification and inhibit a sufficient preconditioning for convection to occur, effectively limiting the spacial extent of events and the volume of produced Labrador Sea Water.

Convective eddies (CE) originate at the rim current of the convective patch. The steep isopycnals along the rim give rise to baroclinic instabilities, generating CEs as a consequence. Their rotation is also anticyclonic, but they feature a cold and fresh core which can be found at mid-depths instead. Observational studies found radii in the range of 5 to $18km$ with maximal azimuthal velocities of 9 to $32cm\,s^{-1}$, appearing smaller and slower than IRs and having mid-depth intensified currents. (Lilly et al., 2003) CEs play a major role in the restratification process, laterally exchanging convected water with water from surrounding regions, causing a heat and buoyancy flux into the convective patch and inducing a rapid restratification (Jones & Marshall, 1997; Rieck et al., 2019).

The last type of eddies found in the Labrador Sea are so called boundary current eddies (BCE), which are caused by smaller baroclinic instabilities along the boundary currents, are only weakly energetic and thus do not propagate very far off-shore (Chanut et al., 2008). Nevertheless, they are considered to be an additional mechanism of transporting heat from the Labrador Current towards the surrounding waters of the convection region and therefore affect the restratification process (Katsman et al., 2004; Chanut et al., 2008).

1.3 Observation and reconstruction methods of mesoscale eddies

Satellite altimetry products are an indispensable resource when it comes to detecting, tracking and characterizing eddies all across the global ocean. However, recent studies show that especially in higher latitudes like in the Labrador Sea, where the deformation radius is small ($\sim 7km$), positions and derived characteristics of eddies do not match shipboard observations (Amores et al., 2018). Two reasons for this are that the spatial resolution of altimetry products is simply not sufficient to capture eddies with radii close

the deformation radius, and secondly, that tracking algorithms tend to misinterpret the signal of multiple small eddies as a single larger one (Amores et al., 2018).
This makes satellite measurements less effective when it comes to examining the eddy-field in the Labrador Sea, which predominantly consists of small and energetic eddies (Lilly et al., 2003). Therefore, most studies rely on in-situ measurements from shipboard observations or data from glider, floats and moorings.

To effectively study an eddy-field, one is usually interested in working out characteristics of the observed eddies, which include their radius, maximum azimuthal velocities and direction of rotation, as well as thermal, haline and density structures. This usually require some sort of transformation of the collected data to create a spacial context, which can be challenging. For example, reconstructing eddies from ship-based observations requires a decomposition of the measured velocities into the radial and azimuthal components of the observed eddy (Castelão & Johns, 2011). In a recent study, Bendinger (2020) developed an elaborate optimization algorithm for this problem, which aims at providing an estimate for the location of an eddy's center based on the measured velocities, which allowed the necessary decomposition and made it possible to reconstruct 14 eddies from shipboard observations.

Similar problems also arise in the evaluation of mooring data. The Eulerian time series captured by a mooring needs to be placed into a spacial context.

First, this requires a method to reliably identify eddy passages in the velocity data. Faced with this problem, Lilly & Rhines (2002) developed a simple, yet effective, analytical method: Continuous plots of the measured velocities on the (u,v) plane - so called hodographs - reveal characteristic geometric structures whenever an eddy passes the mooring. O-shapes indicate the passing of an eddy without slicing its core, D-shapes (perpendicular to the origin) indicate the slicing of an eddy's core and a straight line (perpendicular to the origin) indicates an eddy that has been sliced through its exact center (see Figure 2). This method has been used in a variety of studies to detect or verify eddy passages from mooring data (e.g Bosse et al., 2016; Fan et al., 2013; Lilly et al., 2003);

Secondly, similar to the problem known from ship-based observations, reconstructing the eddy requires knowledge of the advection component, which has to be separated from the signal of the eddy. Estimating the advection component turns out to be very challenging and has been done in many different ways. Here, a new way of separating the advection from the eddy signal will be presented.

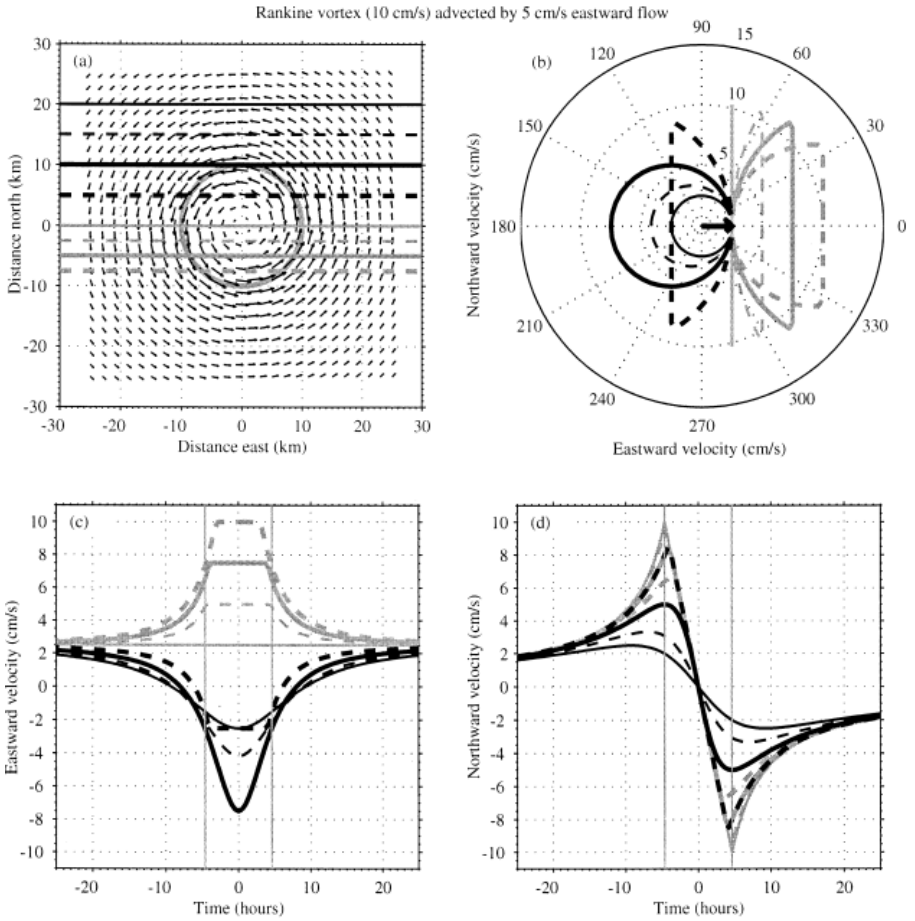

Figure 2: Taken from Lilly & Rhines (2002): (a) Different sections through a model-like cyclonic Rankine vortex, advected by a constant eastward flow; (b) Hodographs of the observed currents for each section; (c & d) matching zonal & meridional velocities for each section

1.4 Study objective

In this study, four years of observations (2016-2020) at the K1 mooring in the central Labrador Sea will be examined for eddy passages based on the methods presented by Lilly & Rhines (2002).

For this, a simple method to automatically detect eddies in the time series of moored velocity observations was developed. Furthermore, general characteristics of any detected eddies are inferred by fitting the observed velocities to a Rankine vortex model in a nonlinear system of equations. The results of the fit are then used to reconstruct exemplary eddies and to estimate their temperature anomalies. Lastly, a classification of the observed eddies is attempted.

2 Data and Methods

2.1 Mooring data

The data used in this thesis comes from a series of moored observations recorded at the K1 mooring in the Central Labrador Sea at around 56.56°N and 52.65°W (Fig. 3). Used here are 2 deployments of the mooring between June 2016 and August 2020, each one covering roughly 2 years of observations.

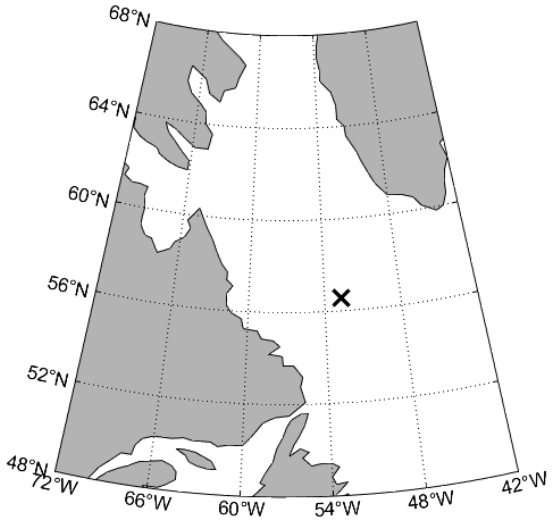

Figure 3: Map of the Labrador Sea; The black cross marks the location of the K1 mooring.

Each mooring was equipped with MicroCATs in various depths, measuring temperature, salinity and pressure every 30 minutes, allowing a reconstruction of the hydrography. Horizontal current velocities were measured with Aquadopp Profilers in $\sim 750m$ and $\sim 1500m$ depth in the same interval. For the second observation period, a third Aquadopp is available near the surface at $\sim 50m$ depth. Additionally, measurements of a Quartermaster ADCP operating at a frequency of $150kHz$ are available, capturing current velocities in the upper $250m$ of the water column in a resolution of $\sim 8m$ at hourly intervals. (see Table 1)

The data from the instruments has been processed and quality controlled as outlined in Zantopp et al. (2017). Temperature, salinity and pressure were corrected using nearby CTD casts from the deployment and recovery cruises and by mounting the instruments to a CTD and making calibration stops at dedicated, full depth calibration stations.

2016-2018			2018-2020		
Depths [m]	Instr.	Measurements	Depths [m]	Instr.	Measurements
0	MicroCAT	T,S,p	5	MicroCAT	T,S,p
25	MicroCAT	T,S,p	8	MicroCAT	T,S,p
90	MicroCAT	T,S,p	49	MicroCAT	T,S,p
242	Quarterm.	u,v,w,p	53	AquaDopp	u,v,p
288	MicroCAT	T,S,p	53	MicroCAT	T,S,p
490	MicroCAT	T,S,p	238	Quarterm.	u,v,w,p
740	MicroCAT	T,S,p	246	MicroCAT	T,S,p
742	AquaDopp	u,v,p	245	MicroCAT	T,S,p
892	MicroCAT	T,S,p	742	MicroCAT	T,S,p
1143	MicroCAT	T,S,p	743	AquaDopp	u,v,p
1295	MicroCAT	T,S,p	892	MicroCAT	T,S,p
1497	MicroCAT	T,S,p	1144	MicroCAT	T,S,p
1498	AquaDopp	u,v,p	1295	MicroCAT	T,S,p
1788	MicroCAT	T,S,p	1497	MicroCAT	T,S,p
1989	MicroCAT	T,S,p	1499	Aquadopp	u,v,p
2193	MicroCAT	T,S,p	1791	MicroCAT	T,S,p
3461	MicroCAT	T,S,p	1991	MicroCAT	T,S,p
			2195	MicroCAT	T,S,p
			3456	MicroCAT	T,S,p

Table 1: Instrumentation of the K1 mooring relevant to this study for both observations periods. Displayed depths are the nominal depths. T for temperature, S for salinity, p for pressure, (u,v,w) for zonal, meridional and vertical current velocities.

2.1.1 Temperature and salinity data

Temperature and salinity measurements from the MicroCATs were boxed by dividing the time-pressure plane into boxes with a size of 3 hours and 30dbar. Each box takes the value of the mean of all measurements that are taken within the respective box. Boxes that only contain one measurement are ignored for statistical reasons and their values are replaced by nans. Because not all depths are covered by the instruments, this procedure is followed by a vertical Akima spline interpolation to fill the missing values.

Only after the interpolation, in-situ temperature and salinity values were converted to conservative temperature and absolute salinity using Gibbs Seawater Library functions (McDougall & Barker, 2011) and the potential density field was calculated.

2.1.2 Velocity data

The velocity data from the Aquadopp instruments contains a strong tidal signal with an amplitude of roughly $5cm\,s^{-1}$ on the semi-diurnal frequency - similar to the case in the Lilly & Rhines (2002) study - which had to be removed from the time series to successfully determine eddies. An initial attempt to remove the tides by applying a low-pass filter to the time series yielded only unsatisfactory results, as residuals of the tides were still visible in the resulting signal.

Instead, a tidal analysis was performed with the help of the t_tide toolbox by Pawlowicz (2002). This was done to calculate a tidal prediction, which is then subtracted from the original time series in an attempt to reduce the tidal noise. Only the two most dominant semi-diurnal constituents (M2, S2) were used for the synthesis of the tidal prediction. After removing the tidal prediction from the original time series, a running mean with a window of 2 days was applied which yielded a much smoother signal than the use of a low-pass filter with a cutoff of the same frequency. It should be noted that this method of filtering a time series reduces the amplitude of strong velocity peaks. This might cause artificially reduced velocities in the evaluation of detected eddies (see Fig. 4). Also, the higher resolution ADCP measurements for the top $250m$ of the water column were interpolated onto a regular vertical grid with a resolution of $10m$.

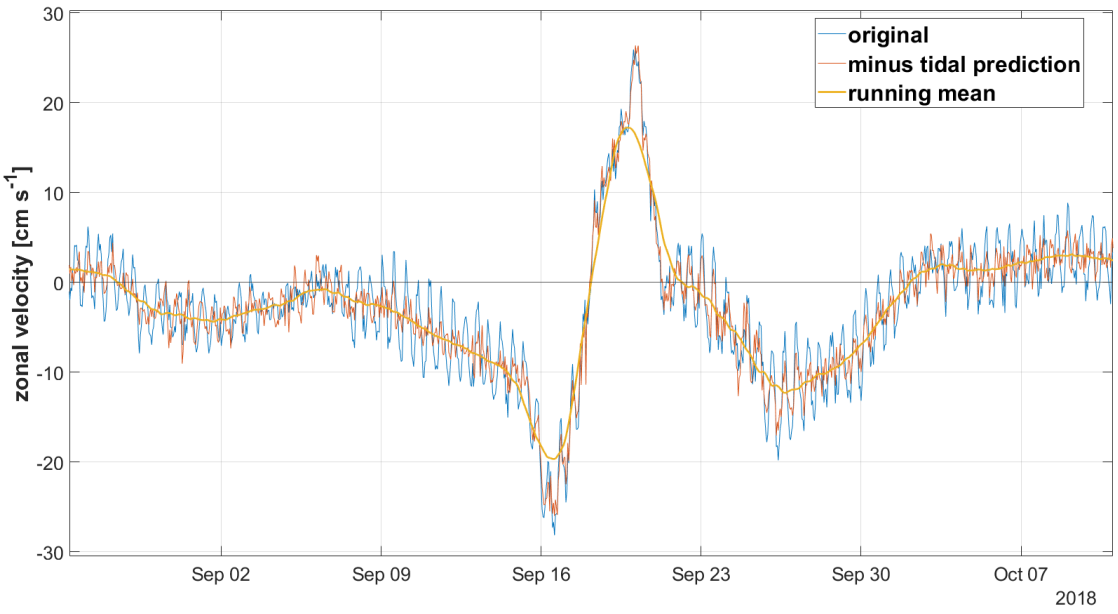

Figure 4: Excerpt of the zonal velocity time series containing an eddy passage. The blue line shows the velocity as recorded, red shows the velocity after removing the tidal prediction and yellow shows the velocity after additionally applying a running mean with a window of 2 days.

2.2 The Rankine vortex model

A Rankine vortex is a circular and radial symmetric flow around a point of origin. The flow field inside its core ($r \leq R$) resembles a solid-body rotation around it's origin, while outside of it's core ($r > R$), the flow is a simple potential vortex, which is free of vorticity (Giaiotti & Stel, 2006). This makes a Rankine vortex a reasonably realistic representation of real eddies. The horizontal velocity field of a Rankine vortex that meets these conditions is defined as

$$U = \begin{cases} U_R * \frac{r}{R}, r \leq R \\ U_R * \frac{R}{r}, r > R \end{cases}$$

,where U_R is the maximum azimuthal velocity, r the distance from the origin, and R the radius of the vortex. U_R is negative (positive) for anticyclones (cyclones) (see Lilly et al., 2003).

In words, the speed in the inner region is proportional to the distance from the origin, while being inversely proportional in the outer region, with the maximum speed observed at the boundary between the two regions ($r = R$). This boundary will be called edge of the eddy in the following and is defined by the radius R.

In this study, the characteristics of a Rankine vortex that has been sliced through its core will be used to develop methods to detect eddies in moored velocity observations, and to infer characteristics by fitting these observations to a model-like Rankine vortex.

Additionally, based on the conceptual model of a Rankine vortex, a simple numerical model has been created to assist with the verification of derived eddy characteristics. This model constructs a Rankine-like velocity field based on the inputs of maximum azimuthal velocity, advection velocity and radius, and allows to display the velocities measured during a section through the eddy in a specified direction and distance from the center. For example, figure 5 shows the velocity field for a stationary Rankine vortex, as well as the velocity components for a west-east section through the core, slicing it north of its center.

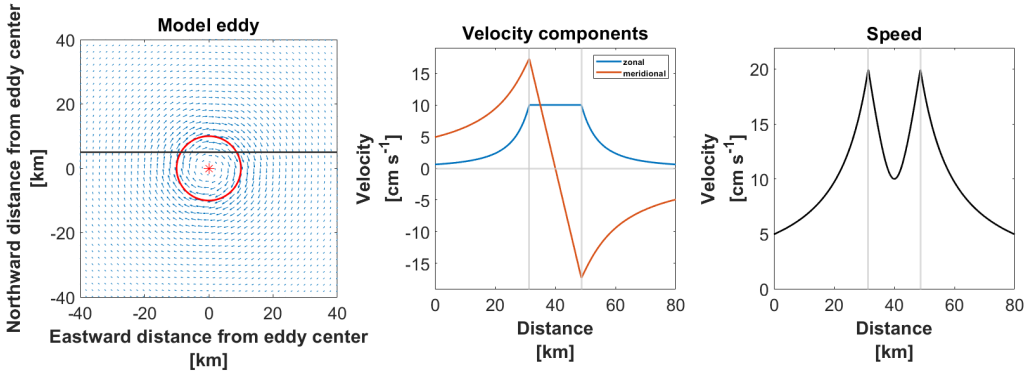

Figure 5: West-East section through a modelled anticylonic Rankine-vortex using the developed numerical model. The constructed eddy and section can be seen on the left. The blue line shows the zonal velocity along the section, orange the meridional and black the speed.

2.3 Eddy detection from moored velocity data

This study focuses on eddies which cores have been sliced by the mooring. Often, these eddies are of most interest, because property anomalies carried by eddies are usually well confined inside its core due to their vorticity structure. The characteristics of a Rankine vortex described in the previous section can be used to define criteria which in turn can be used to identify potential eddies in the velocity data of moored observations.

As per definition of a Rankine vortex, the maximum speeds are found on the edge of the eddy. Therefore, two consecutive peaks in the speed observations within a certain amount of time are likely to be caused by slicing the core on an eddy. One of the peaks emerges when the mooring enters the eddy's core, and the second one when it exits it (see Fig. 5).

Used here are the velocity measurements at $\sim 750m$ depth, as they contain less noise than the uppermost instrument. Peaks in speed are identified using the Matlab function 'findpeaks'. Previous observations in the central Labrador Sea have shown that the maximum azimuthal velocities of almost all eddies exceed $10cm\,s^{-1}$ (Lilly et al., 2003; de Jong et al., 2014). Therefore, any peaks below this value are excluded, as those peaks are almost certainly not caused by an advected eddy. (see Fig. 6(a))

In a second step, any two consecutive peaks are paired, which will be called "double peaks" in the following. Citing the same studies as above, the time a mooring spends inside the core of an eddy usually does not exceed a week. This information is used to exclude any double peaks which were recorded longer than a week apart. (see Fig. 6(b))

In a last step, because not every double peak is necessarily caused by an eddy, two more criteria are set to distinguish double peaks caused by a Rankine vortex from 'random' double peaks. In theory, if a Rankine vortex is advected by a constant mean flow, the

slicing of the eddy happens in the exact opposite direction of the mean flow. This causes a symmetry in the speed signature of an eddy: The peaks always have the same height. For this reason, any double peaks that show a height difference of more than $10cm\,s^{-1}$ in speed are either not caused by an advected eddy or do not have a constant background velocity, which makes it nearly impossible to get good estimates on its characteristics. They are therefore sorted-out. Another feature of a Rankine vortex is that at least one of the velocity components shows a very strong increase or decrease during the passage, which is why it is required that the absolute difference in one of the velocity components between both peaks has to exceed $10cm\,s^{-1}$ in order to be considered an eddy signal. (see Fig. 6(c))

Once again, it should be empathised that this method only considers Rankine-like eddies which cores have been sliced by the mooring and excludes any eddies that only pass it. The criteria chosen to eliminate double peaks are intentionally chosen to be very lenient to avoid excluding any 'true' eddies.

Last, all flagged events were manually reviewed and verified based on the hodograph method from Lilly & Rhines (2002). Any of the potential eddies that either do not show the characteristic D-shape or a straight line in their hodograph, or do not have a clearly defined temperature/density core were also sorted out.

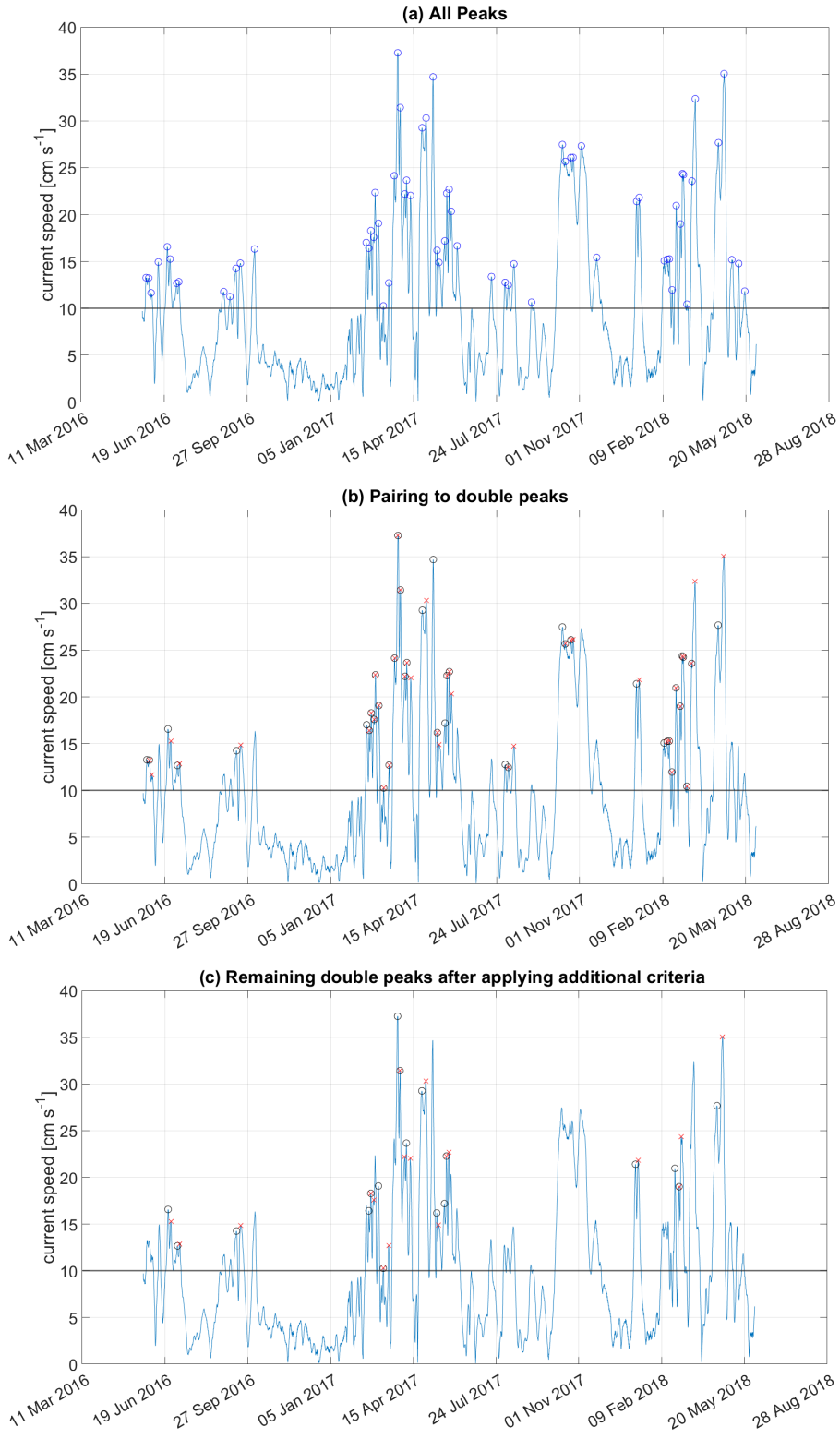

Figure 6: Time series of the observed speed at 750m during the 2016-2018 period. (a) shows all prominent peaks marked by blue circles, (b) shows all pairs of peaks that have been recorded no longer than 7 days apart. The first peak of each pair is marked by a black circle, the second peak is marked by a red cross. (c) shows the remaining pairs after applying additional criteria.

2.4 Deriving eddy characteristics

The observed velocity at the mooring during an eddy's passage consists of two superimposed signals, the advection velocity and the velocity signal of the eddy. To estimate parameters of the eddy, it is necessary to separate the two parts from each other. In the following, the method used in this thesis will be elaborated.

Consider an anticyclonic Rankine vortex with radius R, which is advected with a constant and spacial uniform speed U_{ad} in the direction ϕ past the mooring, so that the mooring slices the core of the eddy in the distance r_{min}. (see Fig. 7)

The speed of a Rankine vortex at any point inside its core is given as $\frac{r}{R} * U_{az}$, where U_{az} is the maximum azimuthal velocity at radius R and r being the distance of the point from the center.

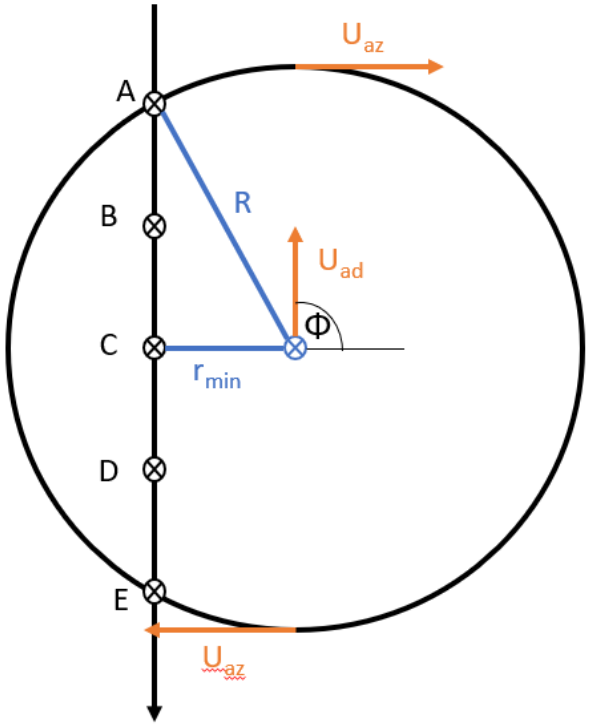

Figure 7: Sketch of an anticyclonic Rankine vortex with a maximum azimuthal velocity U_{az} at radius R, advected in the direction Φ with the constant speed U_{ad}. The mooring slices the eddy on the left side (in opposite direction of the advection/from A to E) in the distance of r_{min} from the center.

The expected velocity $\vec{u}_{obs}$ $(= u_{obs} + iv_{obs})$ at any given point can then be written as the sum of the eddy signal and the advection velocity:

$$U_{ad} * e^{i\phi} + \frac{r}{R} * U_{az} * e^{i(\phi+\Delta\phi)} = \vec{u}_{obs}$$

, where $\Delta\phi$ is the angle difference between the direction of the azimuthal component and the direction of the advection at that point.

The distance between two measuring points can be expressed as $U_{ad} * \Delta t$, where Δt is the time separating them. This makes it possible to express r and $\Delta\phi$ as functions of U_{ad} and r_{min} via simple trigonometry. Written out for each of the 5 measuring points, one yields the following system of equations:

$$U_{ad} * e^{i\phi} + U_{az} * e^{i(\phi - arctan(\frac{2*\Delta t*U_{ad}}{r_{min}}))} - \vec{u}_{obs,A} = 0 \quad (1)$$

$$U_{ad} * e^{i\phi} + \frac{\hat{r}}{R} * U_{az} * e^{i(\phi - arctan(\frac{\Delta t*U_{ad}}{r_{min}}))} - \vec{u}_{obs,B} = 0 \quad (2)$$

$$(U_{ad} + \frac{r_{min}}{R} * U_{az}) * e^{i\phi} - \vec{u}_{obs,C} = 0 \quad (3)$$

$$U_{ad} * e^{i\phi} + \frac{\hat{r}}{R} * U_{az} * e^{i(\phi + arctan(\frac{\Delta t*U_{ad}}{r_{min}}))} - \vec{u}_{obs,D} = 0 \quad (4)$$

$$U_{ad} * e^{i\phi} + U_{az} * e^{i(\phi + arctan(\frac{2*\Delta t*U_{ad}}{r_{min}}))} - \vec{u}_{obs,E} = 0 \quad (5)$$

With $\hat{r} = \sqrt{(\Delta t * U_{ad})^2 + r_{min}^2}$ and $R = \sqrt{(2 * \Delta t * U_{ad})^2 + r_{min}^2}$.

(Note that parts of the system of equations change depending on the rotational sense of the eddy and on which side it is sliced! More about this can be found in the appendix.)

These five equations are now split into their real (zonal) and imaginary (meridional) components, yielding a set of ten equations with four unknowns $(U_{ad}, U_{az}, r_{min}, \phi)$. Since this is an overdetermined, non-linear system of equations, there is no exact solution to this problem. Instead, the variables are fitted to the observational data (measured at the 5 points) by using the least square method, minimizing the errors of the equations above. The results strongly depend on the choice of the initial values. Because of this, for every eddy, this optimization has been done 200 times using varying initial conditions. Sensitivity experiments on how the results of the optimization react to the initial conditions have shown that the quality of the results mostly depend on the choice of the initial velocities U_{az} and U_{ad}, and are best when they are either close to the true value or have a similar ratio. At the same time, low initial values for r_{min} lead to a strong scattering of resulting radii, which can be avoided by choosing a high value instead.

Following Lilly & Rhines (2002) approach, a first estimate for the advection speed is obtained by lowpass-filtering the velocity time series with a Hanning filter with a window 3 times as long as the time between the double peak. This value is randomly varied by up to $\pm 50\%$ for each iteration, as this method tends to be imprecise, especially when the advection is low compared to the eddy signal (see Lilly & Rhines, 2002). The initial value for the azimuthal speed is estimated by taking the average value of the double peak. This value is also randomly varied, but only by up to $\pm 25\%$. Because r_{min} should not be chosen too small, its initial value is set to the apparent radius, calculated as $2 * \Delta t * U_{ad}$, using the first estimate of the advection. Φ can simply be set to the direction of the speed at the center-most point (C), as U_{az} and U_{ad} both point into the direction of advection.

The results of all iterations are then averaged and the standard deviation is calculated. Additionally, the apparant radius is calculated as $2 * \Delta t * U_{ad}$, this time using the result of the optimization.

2.4.1 Temperature anomalies

Here the temperature anomaly is defined as the difference of the vertically averaged temperature inside the eddy at half its radius and the vertically averaged temperature at 1.5 times its radius for the upper $1500m$. Estimates for the two values are derived in the following way:

Inside the eddy, for each measurement point, the distance from the center can be calculated by using the previously determined quantities R and r_{min}. This makes it possible to reference all temperatures to the distance from the center in which they were recorded. Linearly fitting the temperatures to the distances yields a temperature gradient, which can be used to extrapolate an estimate for the temperature in the center of the eddy (see Fig. 8). The evaluation of this linear fit at half the radius is then taken as an estimate for the eddy's average temperature.

The temperature outside the eddy is simply estimated as the vertical average of the measured temperature at 1.5 times the radius. This is done for both sides of the eddy and is then averaged.

The difference between the two estimates then defines the temperature anomaly.

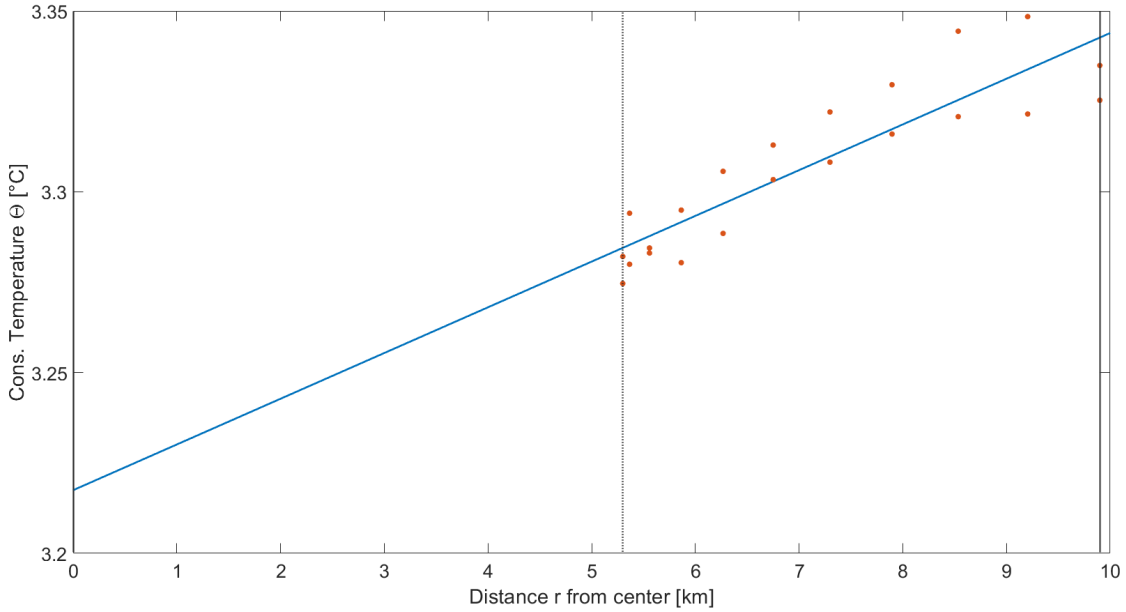

Figure 8: Graphical example for deriving a temperature estimate of eddy 8; The red dots show vertically averaged conservative temperature related to the distance of the measurements from the center. The blue line shows the results of their linear fit. (The dashed vertical line marks r_{min} and the solid vertical line marks radius R)

3 Results and Discussion

3.1 Temperature and velocity time series

Figure 9 shows a stickvector plot and the speed of the observed velocities at mid-depth for the whole observation period, aligned with the time series of the conservative temperature for the upper $2000m$. Unfortunately, the surface waters appear very patchy due to a malfunctioning MicroCAT instrument.

The seasonal cycle of preconditioning, deep convection and restratification is clearly visible in the temperature plot. Preconditioning generally appears to start around late December/January, indicated by the sudden cooling of the surface layer, followed by convection which sets in around February/March, when the buoyancy loss is able to overcome the weak stratification, which is visible in the plot by a vertical homogenisation in temperature of the water column. The warming of the surface at the end of April/May indicates the stop of formation of Labrador Sea water and the water column begins to restratify. The stratification also appears to increase in the following months, which is in line with the findings of Straneo (2006), who argue that the lateral exchange of boundary current water with central Labrador Sea water persist through the entire year.

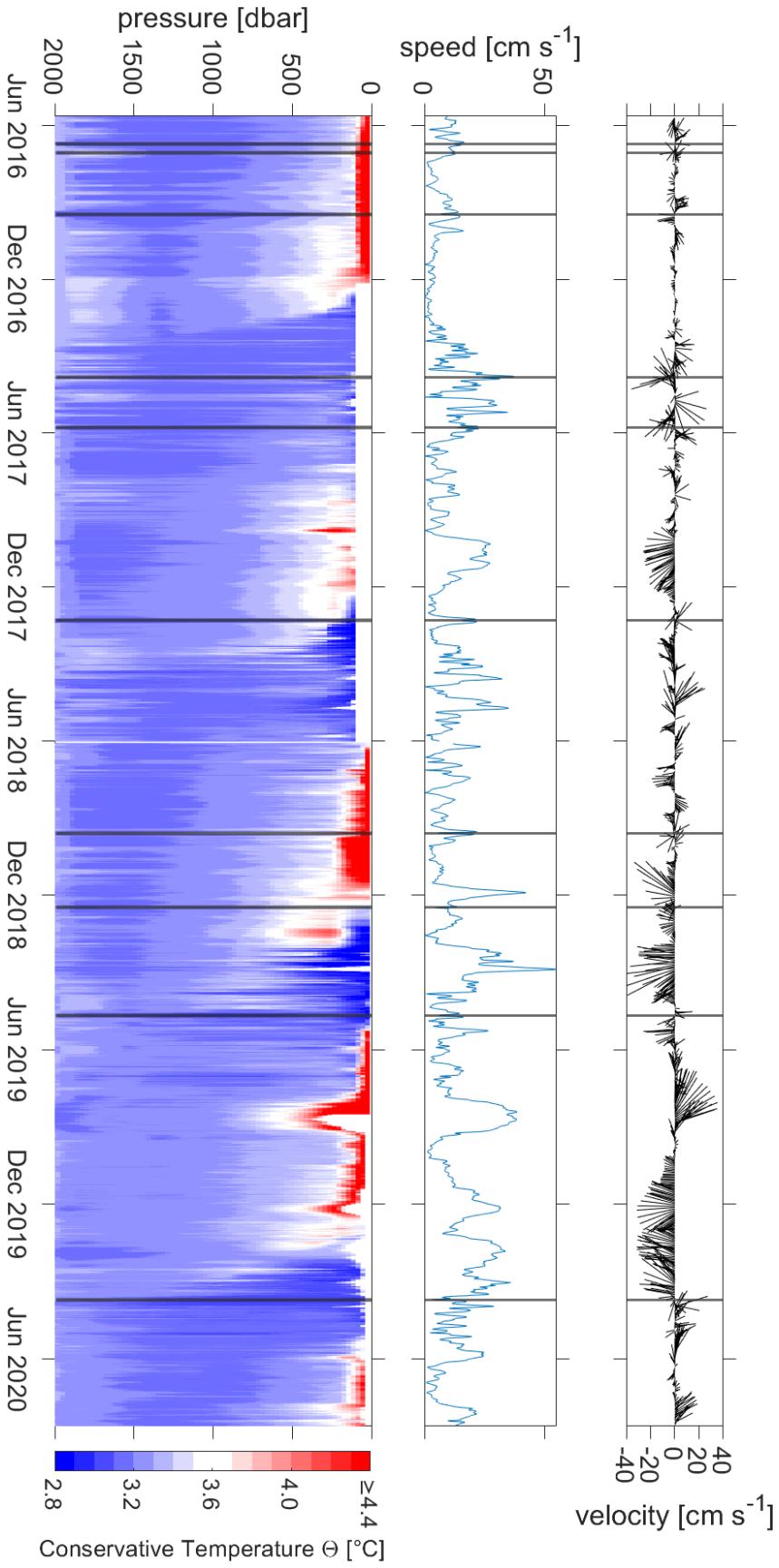

Figure 9: Aligned stickvector plot with current speeds at $\sim 750m$ and conservative temperature in the upper $2000m$ for both observation periods. Found eddy events are marked by vertical black lines.

Usually, these kinds of plots (shown in figure 9) can also be used to detect eddy passages. In a stickvector plot, eddies are characterized by a sudden and short-lived rotation of the vectors, while in speed plots, sliced eddies appear as double peaks as it was discussed in detail in the methods. Additionally, eddies usually show a well structured core of anomalous properties. The black vertical lines indicate all detected events which withstood the manual review and almost all of them coincide with a sudden rotation in the stickvector plot and a double peak in the velocities, which indicates that they are most likely mesoscale eddies. While it is not apparent from this figure, 9 of the 10 eddies show a clearly defined core of anomalous temperatures, supporting this assessment further.

3.2 Eddy detection

The automated detection flagged 29 events as potential eddies, of which only 10 could be verified as eddies after the manual review. The distribution of the ten events over 4 years of observations appears to be relatively even, with 6 detected eddies in the first 2 years and 4 eddies in the last two years. (see Fig. 10) Compared to other studies (Lilly et al., 2003; de Jong et al., 2014), the number of eddies seems to be on the lower end and suggest that some passages might have been missed.

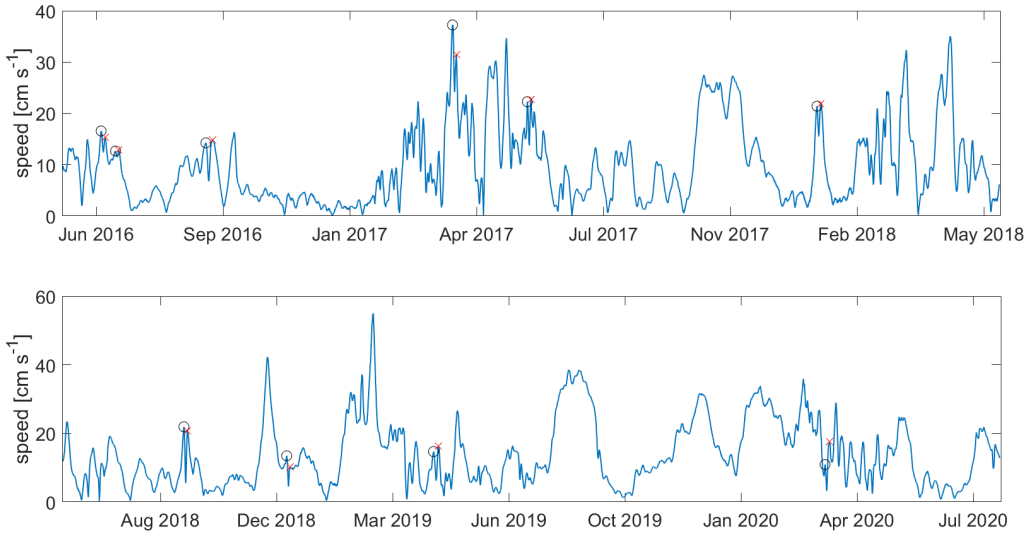

Figure 10: All detected and verified eddy passages in both observation periods. Black circles mark the entering of the mooring into the eddy, red crosses mark its exit.

Most of the falsely flagged events are found between March and May, shortly after convection occurs. For many double peaks which are detected in this period, velocities do not show any identifiable signal in the velocity components or the thermal/density structure that could be interpreted as a mesoscale feature. Some of the other detected but rejected events show weakly defined property anomalies, but no eddy-characteristic

structure in the hodograph, which makes it unlikely that they are coherent eddies.

Additionally, there are some events in the time series that were missed by the automated detection. An example for this is shown in figure 11. Here, one of the flagged events can be seen, followed by a missed event on the 3rd of July, 2019. A well defined cold and fresh core is apparent and the velocity signal resembles that of a Rankine vortex, showing a linear behavior and a strong gradients in the components. In this case, the eddy was not detected because it lacks the first of the two peaks in speed. Most likely, this is caused by a superposition with the prior event, which causes the speed to monotonically decrease over the expected peak on the 2nd of July, so that it can not be detected.

Overall, the method presented in this study is able to detect eddies in the time series data of moored observation. While only about a third of the flagged events could be verified as eddies, it can be used as a tool to 'pre-scan' long time series for potential eddies like in this study, which made the manual search much easier. The method could be improved by implementing another criterion based on the density structure of the eddy. For example, Lilly & Rhines (2002) require a minimum isopycnal displacement of at least $100m$ at $2000m$ depth for an event to be considered as an eddy, which could help in excluding a majority of the false flags, but also cause the exclusion of some true eddies here. Finding the right balance of rejecting as many 'false' eddies as possible while not rejecting 'true' eddies appears to be challenging, which is why a lot of fine-tuning of this method is necessary to reliably detect eddies automatically.

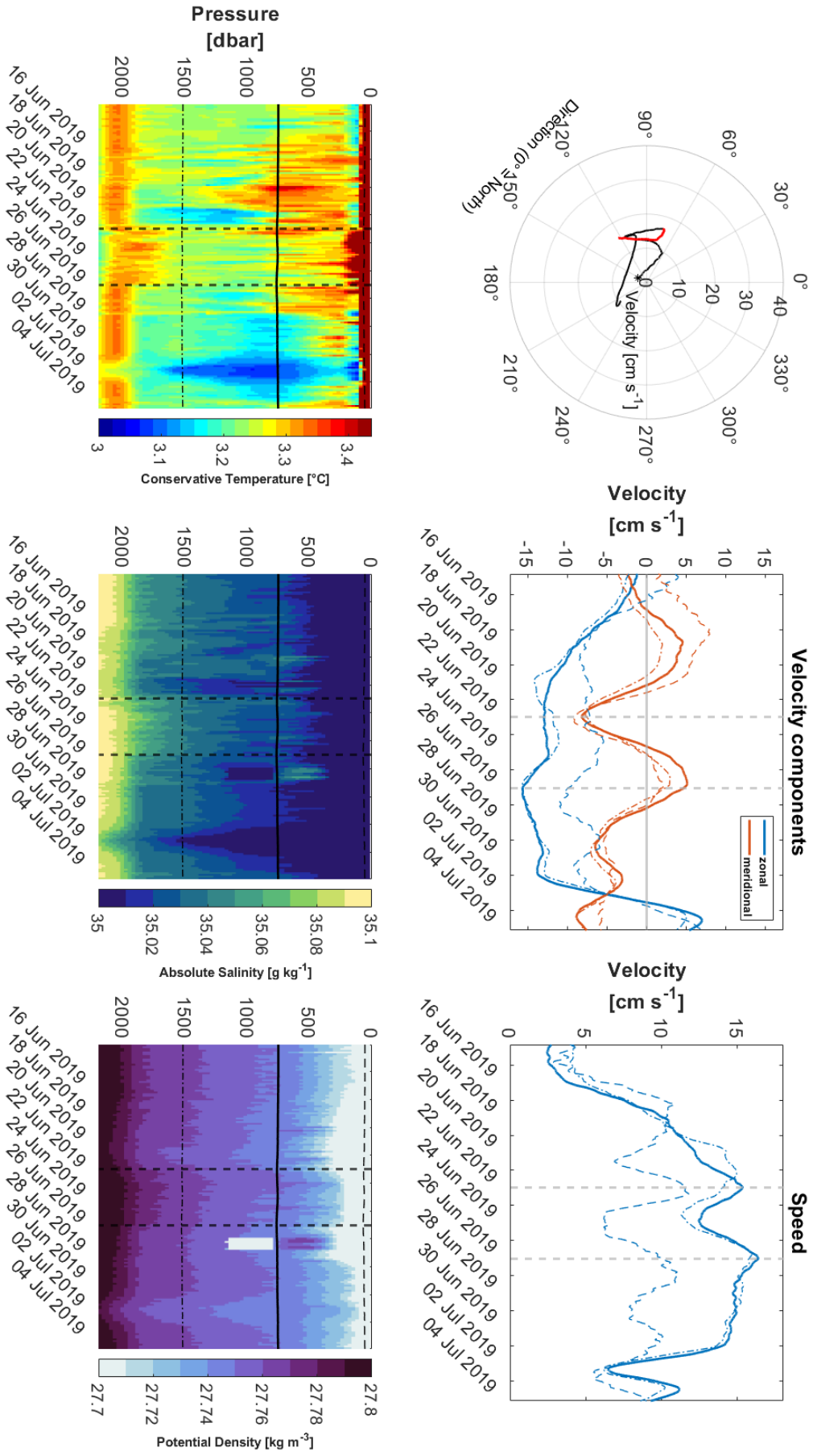

Figure 11: Caption next page.

Figure 11: Excerpt, showing a flagged event next to a missed event on the right. Top left shows the hodograph, top shows the velocity components, blue for zonal and orange for meridional, top right shows the speed. The core of the eddy is marked by vertical dashed lines and appears red in the hodograph. The lower panes show conservative temperature, absolute salinity and potential density respectively. The location of the velocity measurements are marked by horizontal lines.

3.3 Eddy properties and characteristics

The characteristics of the ten eddies have been derived by fitting their observed velocities to a Rankine vortex as described in the methods. The results of this fit can be found in Table 2. The quality of the results can be assessed by reconstructing the eddies based on the derived characteristics in the developed numerical model and comparing the resulting theoretical velocities to the observational data. Overall, the reconstructed velocities fit the observations quite well. An exception to this are the eddies which have been sliced relatively far from the center, which also appear to have higher standard deviations in their derived characteristics. This means that these eddies are more sensitive to the initial conditions and their results should not be taken at face value.

Nr.	Rot.	U_{az}	U_{ad}	r_{min}	R	X	Δt	ΔT
1	A	15.6 (0.3)	7.1 (1.5)	1.6 (0.6)	10.5 (2.0)	10.4	81	-0.06
2	C	19.4 (1.3)	6.8 (1.5)	11.3 (3.4)	13.5 (3.7)	7.4	60.5	0.01
3	A	19.8 (0.6)	6.9 (0.9)	13.1 (2.4)	20.3 (3.0)	15.6	126	-0.09
4	A	28.9 (0.3)	13.2 (0.8)	7.7 (0.1)	18.9 (0.9)	17.2	72.5	-0.09
5	A	29.7 (0.5)	9.1 (0.9)	8.4 (1.2)	14.0 (1.5)	11.2	68.5	-0.11
6	A	30.2 (1.1)	9.6 (1.5)	12.7 (2.8)	18.0 (3.4)	12.8	74	-0.17
7	C	25.3 (0.2)	8.1 (0.3)	5.3 (0.3)	11.9 (0.5)	10.6	73	0.23
8	A	14.6 (0.1)	5.9 (0.1)	3.7 (0.1)	7.8 (0.2)	6.9	64.5	-0.07
9	A	16.6 (0.1)	2.4 (0.7)	0.4 (0.1)	4.5 (1.2)	4.5	104	-0.07
10	C	13.0 (2.4)	12.6 (2.8)	19.7 (1.1)	23.1 (1.2)	11.8	52	0.00

Table 2: Eddy characteristics derived from fitting observed velocities to a Rankine model. Values are means of 200 iteration using varying initial conditions, values in the brackets denote the standard deviation. Rot. is the rotational sense of the eddy, either (C) cyclonic or (A) anticyclonic, U_{az} is maximum azimuthal speed $[cm\,s^{-1}]$, U_{ad} is advection speed $[cm\,s^{-1}]$, r_{min} is the distance of the section from the eddy's center $[km]$, R is the radius $[km]$, X is the apparant radius $[km]$, Δt is the duration the mooring stayed inside the core $[h]$ and ΔT is the vertically averaged temperature anomaly in the top $1500m$ $[°C]$.

Of the ten eddies, seven show an anticyclonal and three a cyclonal rotation. All of the anticyclonal eddies feature a cold and fresh core, while the cyclones show warm and saline cores. The number of cyclones found in this study is unusual, as in previous studies, only very few cyclones in the central Labrador Sea have been detected and described, all featuring warm and saline cores (Lilly & Rhines, 2002). For the anticyclones, the temperature anomalies lie in a range of -0.06 and $-0.17°C$. Only one of the cyclones shows a significant temperature anomaly of $+0.23°C$, but that might be because the other two were sliced very far on the outside, so their estimates could be faulty.

In the following, three of the observed eddies are examined in more detail.

Eddy 1 (Fig. 12) is an anticyclonic cold-core eddy with a radius of $10.5km$ which has been sliced closed to its center. The cold and fresh core extends from the subsurface waters to $2200m$ depth, with isopycnals bending around it. Notably eddy 3 and 6 have a very similar structure, but show greater radii and azimuthal velocities. While it could be argued that these are convective eddies, the core is usually well confined to mid-depths, which is not the case here.

On first sight, eddy 7 (Fig. 13) appears like an Irminger Ring based on its warm saline core and its high azimuthal velocity of $25.3cm\,s^{-1}$. With a radius of $12km$ it would be a relatively small one, but it still fits into the range of 11 to $35km$ reported in de Jong et al. (2014), who did an extensive study on these kind of eddies. However, this particular eddy appears to be cyclonic from the velocity signature and its hodograph. It shows only a very weak flow towards the surface, notable in the speed plot and in the (non-depicted) ADCP measurements in the top $250m$. Furthermore, the measured speeds intensify with depth and is highest at the lowest instrument. This stands in contrast to previous observations who report intensified surface currents for IRs (Lilly et al., 2003; de Jong et al., 2014). Its velocity and density structure resembles more that of depth-intensified cyclones found in the convective regions of the Mediterranean Sea (Bosse et al., 2016).

Eddy 8 (Fig. 14) can be described as an anticyclonic mode-water eddy with the radius of $7.9km$, which has a clearly defined cold $(-0.4°C)$ and fresh $(0.2g\,kg^{-1})$ core which extends from 500 to $1250m$ and shows the highest speeds of $14.6cm\,s^{-1}$ at mid-depth. This description fits almost perfectly with prior observations of convective eddies (Lilly & Rhines, 2002), with the difference that this one appears even more confined to the mid-depths. Interestingly, this eddy was observed in December 2018, about 8 months after the deep convection-event, which indicates a long life span of convective eddies. Similar observations were made by Lilly et al. (2003), who detected convective eddies with

double cores, which show a shallow core of newly convected waters above a deeper core of convected waters from the previous year and are argued to be created due to eddy-eddy interactions. This indicates that the lifespan of convective eddies can extend a year.

Despite their common occurrence in other studies (Lilly et al., 2003, de Jong et al., 2014), no eddies of the type 'Irminger Ring' were detected during the observation period. Contrarily, an uncommon amount of warm cyclones were identified, which have only rarely been recorded and described. Lilly & Rhines (2002) also detected two warm-core cyclones with similar characteristics as eddy 7 at "Bravo", right next to the K1 mooring. While cyclonic counterparts to Irminger Rings exist, altimeter studies suggest that they decay fast as they move away from their formation region (Lilly et al., 2003). It cannot be ruled out that the eddy found in this study is an exemption to this.

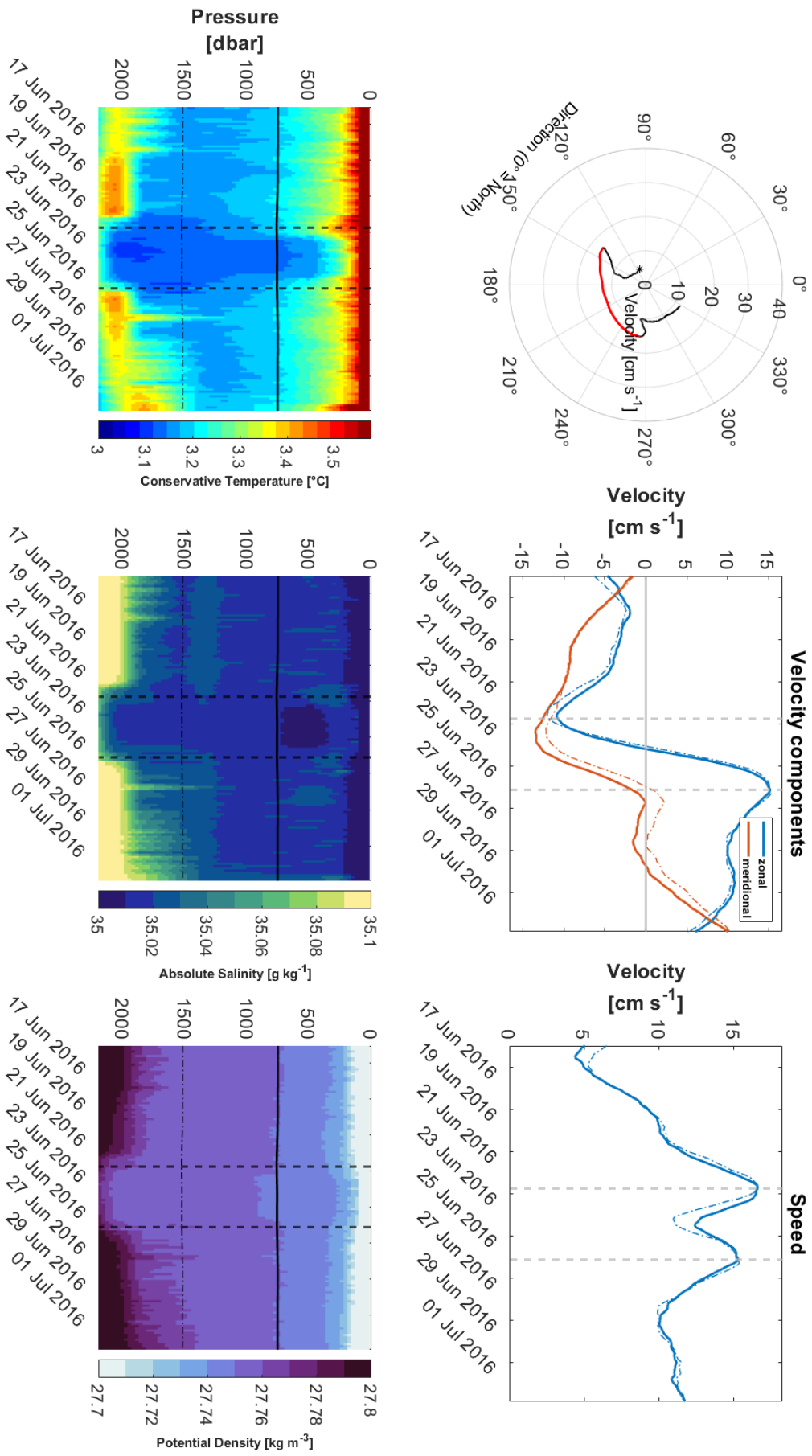

Figure 12: Eddy 1: Anticyclonic cold-core eddy. Description of the plots are found in the caption of figure 11.

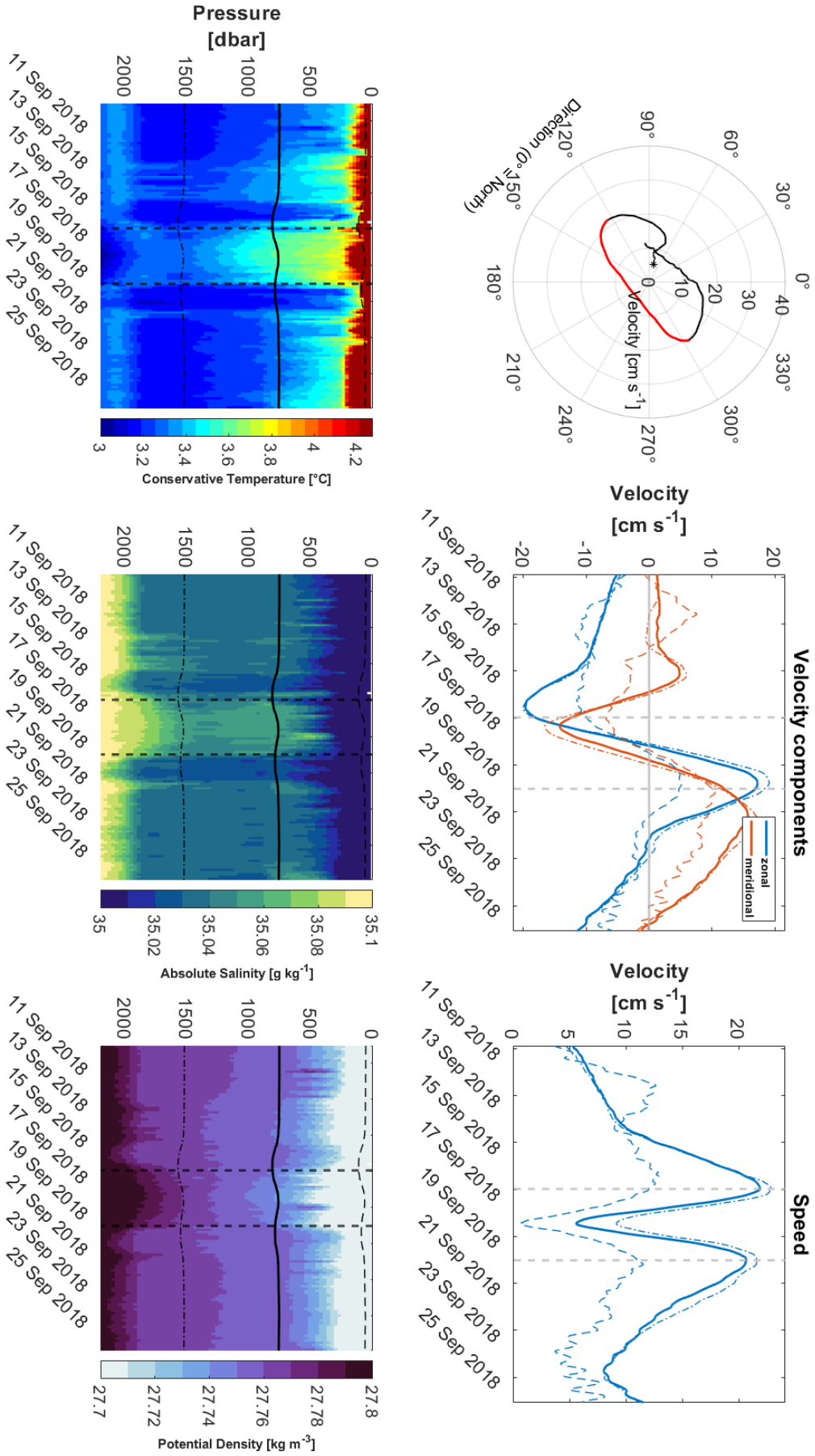

Figure 13: Eddy 7: Cyclonic warm-core eddy. Description of the plots are found in the caption of figure 11.

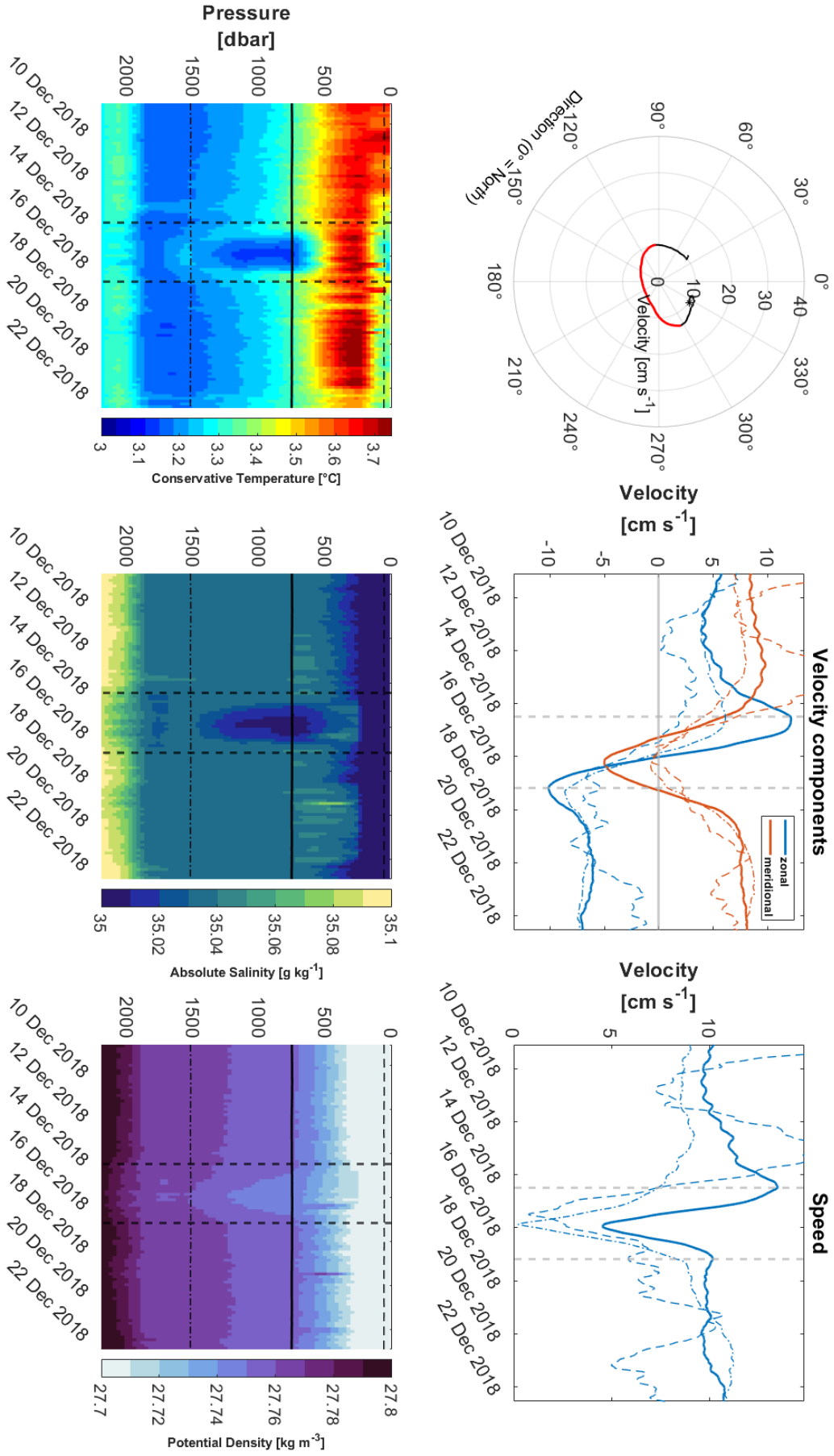

Figure 14: Eddy 8: Anticyclonic mode water eddy. Description of the plots are found in the caption of figure 11.

4 Summary and Conclusion

Four years worth of time series data from the K1 mooring in the Central Labrador Sea have been examined for eddy occurrences. To identify eddy passages in the velocity data of moored instruments, a simple semi-automated method was developed, in which the recorded velocities were searched for signals that resemble the characteristic signal one would get by slicing the core of a Rankine vortex. Overall, the programm detected 29 events, of which 10 were identified as eddies in a manual review based on their hodographs and hydrographic structure.
The characteristics of all identified eddies were inferred by fitting their observed velocities to a model-like Rankine vortex in a non-linear system of equations. The results were quality controlled by reconstructing the eddie based on the derived charactersitics in a simple numerical model and comparing the obtained velocities from that model to the observations.

From the ten eddies detected, three show a cyclonic rotation which are unusually many compared to previous studies (e.g. Lilly et al., 2003). One of them shows depth-intensified currents, which has not been observed in this region, but in the deep convection region of the Gulf of Lyon (Bosse et al., 2016). It can be assumed to be the cyclonic counterpart of an Irminger Ring. No IRs have been detected in this study which stands in contrast to prior observations in which they appear to be a common feature (Lilly et al., 2003; de Jong et al., 2014). One anticyclone has been classified as a Convective Eddy, which has been detected 8 months after convection, indicating a long live-span of CEs. The absense of the common types of eddies and the presence of eddies with structures which haven't been described so far suggests that the eddy-field is more complicated than other studies might indicate and highlights the importance of observational studies when it comes to characterizing an eddy-field.

While the eddy detection method presented in this study was helpful to pre-scan the long time series for potential eddy events, the exclusion criteria need tweaking to find the right balance of sorting out as many 'false flags' as possible without rejecting actual eddies. Once this is done, this might be a great tool to automatically detect eddies in moored velocity time series. The method used to derive eddy characteristics provides good estimates, but the results are also highly dependent on the first estimate of the initial condition. This is especially true for eddies which have been sliced far away from its center, as they appear more sensitive to small changes in the initial condition. The derived and displayed values should therefore be taken with a grain of salt.

Ultimately, studies of mesoscale eddies are critical to understand heat and freshwa-

ter fluxes from the boundary currents into the central Labrador Sea. Characteristics of eddies can be used to get reliable estimates for the heat anomalies confined in the core of the eddy: Because both, radius and distance of the section from the center are estimated, every measured temperature can be referenced to the distance from the center. Linearly fitting the temperatures provides an estimate of the temperature distribution for the entire eddy (see Fig. 8), which can be calculated into heat anomalies when compared to the outside. While this is not done here, future studies could expand on this.

5 Appendix

Here it is discussed how the system of equations needs to be adapted for different slices through a Rankine vortex. The four cases are depicted in Figure 15. Case (a) has already been discussed in detail in the methods part. There are two possible changes to consider, depending on which scenario is present.

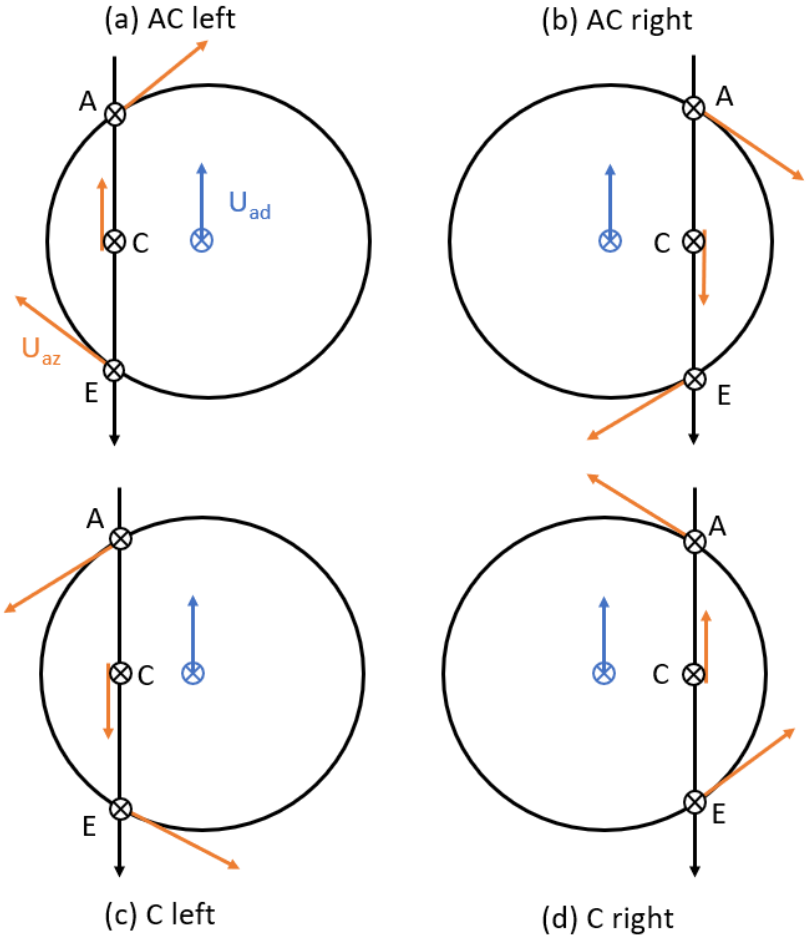

Figure 15: The four different cases to consider: (a) anticyclone sliced on the left, (b) anticyclone sliced on the right, (c) cyclone sliced on the left and (d) cyclone sliced on the right.

(1) In the case an anticylone is sliced on the right side of its center (b), or a cyclone is sliced on the left (c), U_{az} and U_{ad} show in opposite directions at the center-most point and not in the same anymore. This needs to be considered in the initial equation which changes from:

$$U_{ad} * e^{i\phi} + \frac{r}{R} * U_{az} * e^{i(\phi+\Delta\phi)} = \vec{u}_{obs}$$

to

$$U_{ad} * e^{i\phi} + \frac{r}{R} * U_{az} * e^{i(-\phi+\Delta\phi)} = \vec{u}_{obs}$$

(2) The second important thing to consider the sign of $\Delta\phi$ at each point. For the cases (a) and (c), the angle of the azimuthal velocity increases from A to E. Because C is the reference point, the angle is smaller for point A, so $\Delta\phi$ is negative, and bigger for point E, so $\Delta\phi$ is negative. For cases (b) and (d), it is exactly the other way around.

This leads to 4 different systems of equations for the optimization problem. Which case is present can usually be inferred from the hodograph alone, unless the direction of advection is not accessible. Where this is the case, the temperature and density field is used to determine the rotation of the eddy, after which the case is clearly identifiable from the hodograph.

6 References

Amores, A., Jordà, G., Arsouze, T., and Le Sommer, J. (2018): Up to what extent can we characterize ocean eddies using present-day gridded altimetric products? *Journal of Geophysical Research: Oceans*, 123, 7220–7236.

Bendinger, A. (2020): Characteristics of Mesoscale and Submesoscale Eddies in the Labrador Sea: Observations vs. Model. Master thesis. Christian-Albrechts-University, Kiel, Germany

Bosse, A., et al. (2016): Scales and dynamics of Submesoscale Coherent Vortices formed by deep convection in the northwestern Mediterranean Sea. *J. Geophys. Res. Oceans* , 121, 7716– 7742.

Castelão, G. P., and Johns, W. E. (2011): Sea surface structure of North Brazil Current rings derived from shipboard and moored acoustic Doppler current profiler observation. *J. Geophys. Res.*, 116, C01010.

Chanut, J., Barnier, B., Large, W., Debreu, L., Penduff, T., Molines, J. M., & Mathiot, P. (2008): Mesoscale Eddies in the Labrador Sea and Their Contribution to Convection and Restratification. *Journal of Physical Oceanography*, 38(8), 1617-1643.

Clarke, R. A., & Gascard, J. (1983): The Formation of Labrador Sea Water. Part I: Large-Scale Processes. *Journal of Physical Oceanography*, 13(10), 1764-1778.

Cuny, J., Rhines, P. B., Niiler, P. P., & Bacon, S. (2002): Labrador Sea Boundary Currents and the Fate of the Irminger Sea Water. *Journal of Physical Oceanography*, 32(2), 627-647.

de Jong, M. F., Bower, A. S., & Furey, H. H. (2014): Two Years of Observations of Warm-Core Anticyclones in the Labrador Sea and Their Seasonal Cycle in Heat and Salt Stratification. *Journal of Physical Oceanography* , 44(2), 427-444.

Eden, C., & Böning, C. (2002): Sources of Eddy Kinetic Energy in the Labrador Sea. *Journal of Physical Oceanography*, 32(12), 3346-3363.

Fan, X., Send, U., Testor, P., Karstensen, J., & Lherminier, P. (2013): Observations of Irminger Sea Anticyclonic Eddies. *Journal of Physical Oceanography*, 43(4), 805-823.

Gascard, J., & Clarke, R. A. (1983): The Formation of Labrador Sea Water. Part II. Mesoscale and Smaller-Scale Processes.*Journal of Physical Oceanography*, 13(10), 1779-1797.

Giaiotti, D. B., & Stel, F. (2006): The Rankine vortex model. Ph.D. course on environmental fluid mechanics. *Italy: University of Trieste, International Centre for Theoretical*

Physics.

Hátún, H., Eriksen, C. C., & Rhines, P. B. (2007): Buoyant Eddies Entering the Labrador Sea Observed with Gliders and Altimetry. *Journal of Physical Oceanography* , 37(12), 2838-2854.

Jones, H., & Marshall, J. (1997): Restratification after Deep Convection. *Journal of Physical Oceanography* , 27(10), 2276-2287.

Katsman, C. A., Spall, M. A., & Pickart, R. S. (2004): Boundary Current Eddies and Their Role in the Restratification of the Labrador Sea. *Journal of Physical Oceanography* , 34(9), 1967-1983.

Lavender, K., Davis, R. & Owens, W. (2000): Mid-depth recirculation observed in the interior Labrador and Irminger seas by direct velocity measurements. *Nature*, 407, 66–69.

Lilly, J. M., & Rhines, P. B. (2002): Coherent Eddies in the Labrador Sea Observed from a Mooring. *Journal of Physical Oceanography*, 32(2), 585-598.

Lilly, J. M., Rhines, P. B., Schott, F., Lavender, K., Lazier, J., Send, U., and D'Asaro, E. (2003): Observations of the Labrador Sea eddy field. *Progress in Oceanography*, 59(1), 75–176.

Marshall, J., and Schott, F. (1999): Open-ocean convection: Observations, theory, and models. *Rev. Geophys.*, 37(1), 1–64.

Pickart, R. S., Torres, D. J., & Clarke, R. A. (2002): Hydrography of the Labrador Sea during Active Convection. *Journal of Physical Oceanography*, 32(2), 428-457.

Rieck, J. K., Böning, C. W., & Getzlaff, K. (2019): The Nature of Eddy Kinetic Energy in the Labrador Sea: Different Types of Mesoscale Eddies, Their Temporal Variability, and Impact on Deep Convection. *Journal of Physical Oceanography*, 49(8), 2075-2094.

Straneo, F. (2006): Heat and Freshwater Transport through the Central Labrador Sea. *Journal of Physical Oceanography*, 36(4), 606-628.

Treguier, A. M., Theetten, S., Chassignet, E. P., Penduff, T., Smith, R., Talley, L., Beismann, J. O., & Böning, C. (2005): The North Atlantic Subpolar Gyre in Four High-Resolution Models. *Journal of Physical Oceanography*, 35(5), 757-774.

Zantopp, R., Fischer, J., Visbeck, M., and Karstensen, J. (2017): From interannual to decadal: 17 years of boundary current transports at the exit of the Labrador Sea. *J. Geophys. Res. Oceans*, 122, 1724– 1748.

Used toolboxes:

t_tide toolbox, based on

Pawlowicz, R., B. Beardsley, and S. Lentz, "Classical Tidal Harmonic Analysis Including Error Estimates in MATLAB using T_TIDE", *Computers and Geosciences*, 2002.

gsw_library toolbox, based on

McDougall, T.J. and P.M. Barker, 2011: Getting started with TEOS-10 and the Gibbs Seawater (GSW) Oceanographic Toolbox, 28pp., SCOR/IAPSO WG127, ISBN 978-0-646-55621-5.

List of external figures:

Figure 1: Chanut, J., Barnier, B., Large, W., Debreu, L., Penduff, T., Molines, J. M., & Mathiot, P. (2008): Mesoscale Eddies in the Labrador Sea and Their Contribution to Convection and Restratification. *Journal of Physical Oceanography*, 38(8), 1617-1643, Figure 1

Figure 2: Lilly, J. M., & Rhines, P. B. (2002): Coherent Eddies in the Labrador Sea Observed from a Mooring. *Journal of Physical Oceanography*, 32(2), 585-598, Figure 7.

Declaration

I confirm that the master thesis "Characterizing mesoscale eddies in the Labrador Sea based on data from moored observations" is the result of my own work. No other person's work has been used without acknowledgement in the main text of this thesis. This thesis has not been submitted for the award of any other degree or thesis in any other institution.

All sentences or passages quoted in this thesis from other people's work have been specifically acknowledged by clear cross-referencing. Any illustrations which are not the work of the author of this thesis are specifically acknowledged.

The submitted written version of the thesis corresponds to the version on the electronic storage device (filename: 'Kunst_1105582').

Place & Date	Tobias Kunst